Three-dimensional superconductivity induced by an extremely small amount of Li in Li_xSnSe_2

Daniel Duong,[1] Jie Xing,[1] Eklavya Thareja,[2] Silu Huang,[1] Scott Crittenden,[1]
William A. Shelton,[2] and Rongying Jin[1,*]

[1]*SmartState Center for Experimental Nanoscale Physics, Department of Physics and Astronomy, University of South Carolina, Columbia, South Carolina 29208, USA*

[2]*Department of Physics and Astronomy, Louisiana State University, Baton Rouge, Louisiana 70803, USA*

(Received 2 February 2024; revised 22 March 2024; accepted 7 June 2024; published 20 June 2024)

Unconventional superconductivity occurs often in materials with low dimensionality. Here, we report superconductivity observed in layered Li_xSnSe_2 with the superconducting transition temperature $T_c \sim 6$ K. Through Li^+ intercalation in semiconducting $SnSe_2$ via electrochemical process, Li_xSnSe_2 is formed with an extremely small x value as estimated from the c-axis lattice parameter, carrier concentration, and first-principles calculations. Electrical resistivity and magnetic susceptibility measurements allow the construction of both lower (H_{c1}^{ab}) and upper critical field (H_{c2}^{ab} and H_{c2}^{c}) phase diagrams. While H_{c2}^{c} obtained from 10% and 50% resistivity drops exhibits linear temperature dependence, H_{c2}^{c} (90% resistivity drop), H_{c1}^{ab}, and H_{c2}^{ab} can be described by the empirical formula $H_{ci}(T) = H_{ci}(0)[1 - (\frac{T}{T_{c0}})^2]$ ($i = 1, 2$), giving $H_{c2}^{c}(0) = 754$ Oe, $H_{c1}^{ab}(0) = 27$ Oe, and $H_{c2}^{ab}(0) = 1652$ Oe. Using the Ginzburg-Landau formula, we further estimate that the c-axis penetration depth $\lambda_c(0) = 396$ nm and the coherence length anisotropy $\xi_{ab}(0) = 66.1$ nm and $\xi_c(0) = 30.3$ nm. The fact that $\xi_c(0)$ is much longer than the interlayer separation implies three-dimensional superconductivity with superconducting anisotropy $\xi_{ab}(0)/\xi_c(0) \sim 2.2$.

DOI: 10.1103/PhysRevB.109.224512

I. INTRODUCTION

Superconductivity has been a forefront subject of Condensed Matter Physics for over a century. Superconductors with layered structures are of particular interest due to the variety of unconventional characteristics such as high superconducting transition temperature (T_c), structure manipulation, and interplay between superconductivity and magnetism. For example, cuprate superconductors have critical temperatures much higher than those predicted by the Bardeen-Cooper-Schrieffer (BCS) theory [1]. Infinite layer nickelates and Fe-based superconductors have unique magnetic interplay via competition between the superconducting state and long-range magnetic ordering [2,3]. Twisted bilayer graphene with rotational offsetting of the layers induces superconductivity [4]. The recent discovery of high-T_c superconductivity in $La_{n+1}Ni_nO_{3n+1}$ ($n = 2$ and 3) under pressure generates further excitement in this subject [5,6].

Superconductivity in layered materials is mostly obtained via chemical doping through high temperature synthesis or the application of external pressure [1–6]. A much less popular approach is through intercalation under ambient condition, which typically expands the interlayer spacing. This technique allows one to insert atoms or molecules within or between the layers of a host material. For example, the insertion of a H_2O molecule into $Na_{0.3}CoO_2$ results in superconductivity with $T_c \sim 5$ K and more than doubled interlayer spacing [7,8]. In the conventional wisdom, the enhanced two dimensionality in such a system favors the formation of superconductivity with possible unconventional pairing mechanisms including d-, p-, and f-wave symmetries [9–12]. While similar pairing symmetries are proposed for superconducting Li_xSnSe_2 [13,14], there is no clear trend on the relationship between superconductivity and crystal dimensionality as there are a few layered materials, such as $TiSe_2$ [15–20] and $SnSe_2$ [21–24], that can host superconductivity via either enhancing the two dimensionality through intercalation or squeezing the lattice through external pressure. It is considered that the interlayer Se-Se bonding plays a key role for pressure-induced superconductivity [25], which is obviously disadvantageous for intercalated systems that enhance the Se-Se separation. Understanding the relationship between the crystal structure, effective dimensionality, and superconductivity in such systems is extremely important for discovering new superconductors and/or pairing mechanisms.

Despite reported superconducting properties in $SnSe_2$ hosted superconductors with various intercalants, unique features are not properly addressed such as the role of the interlayer spacing and intercalants (nonmagnetic versus magnetic) in superconductivity, linear temperature dependence of the upper critical field H_{c2} [22–24], and normal-state behavior. In addition, most of the published experimental work was carried out in thin flakes and thin films, which makes the theoretical modeling difficult due to the small superconducting volume. In this article, we report experimental and theoretical investigations of both host material ($SnSe_2$) and Li intercalated $SnSe_2$ (i.e., Li_xSnSe_2) single crystals. We compare their electronic and magnetic properties in both the in-plane and out of plane directions in a wide temperature and field range,

*Contact author: rjin@mailbox.sc.edu

providing the insight on the origin of superconductivity in Li_xSnSe_2 induced by an extremely small amount of Li intercalation.

II. SINGLE-CRYSTAL GROWTH, EXPERIMENTAL CHARACTERIZATION METHODS, AND CALCULATION TECHNIQUES

The single crystals of $SnSe_2$ were grown using the modified Bridgman method. The elemental Sn shots (99.99+%, Alfa Aesar) and Se powder (99.999%, Alfa Aesar) with a molar ratio of Sn:Se = 1:2 were sealed in evacuated quartz tubes. The tubes were heated at a rate of 60 °C/h up to 900 °C and held at this temperature for 24 h. The mixture was then slowly cooled (–2 °C/h) to 200 °C and then to room temperature by turning off the furnace. Platelike single crystals with a typical surface area of 4 mm × 4 mm were obtained, which are stable in air. For Li_xSnSe_2 superconductors, dc current was applied between the Pt anode and $SnSe_2$ crystals which were submerged in a lithium hexafluorophosphate ($LiPF_6$) solution (Sigma-Aldrich). The current (5–200 μA), solution (0.1–1.0 *M*), and duration (2–12 h) were tuned for changing the x value.

As-grown and intercalated crystals were examined using a Rigaku Ultima IV x-ray diffractometer with Cu $K\alpha_1$ radiation ($\lambda = 1.5406$ Å). Electrical resistivity, Hall effect, and specific heat measurements were carried out on a Quantum Design Physical Property Measurement System (PPMS Dynacool, 14 T). The electrical resistivity and Hall effect were measured using the standard four-probe method. Data below 1.8 K were obtained in a dilution refrigerator with an 18 T superconducting magnet at National High Magnetic Field Laboratory (Tallahassee, Florida). Magnetic susceptibility measurements were carried out on a Quantum Design Magnetic Property Measurement System (MPMS XL).

The structural and electronic properties of Li_xSnSe_2 (x = 0, 0.52%, 1.2%, and 3.6%) were calculated using the Vienna *Ab Initio* Simulation Package (VASP) [26–29]. The projector-augmented wave (PAW) pseudopotentials [30] with the Perdew-Burke-Ernzerhof (PBE) exchange-correlation functional [31] were employed for Li ($1s^2$, $2s^1$), Sn ($4d^{10}$, $5s^2$, $5p^2$), and Se ($4s^2$, $4p^4$). In addition, van der Waals (vdW) interactions were treated using the semiempirical density functional theory (DFT)-D2 method of Grimme [32]. Other methods including semiempirical DFT-D3 [33,34], the Tkatchenko-Scheffler method with iterative Hirshfeld partitioning [35,36], and the nonlocal vdW functionals optB88 [37] and optB86b [38], as well as both meta-GGA SCAN [39] and r^2SCAN [40] DFT combined with rVV10, were investigated.

III. RESULTS AND DISCUSSION

To determine the crystal structure, as-grown single crystals were ground into powder for x-ray diffraction (XRD) measurements. The XRD pattern is consistent with those reported earlier [41,42], corresponding to the $P-3m1$ space group. A schematic of the crystal structure of $SnSe_2$ is shown in Fig. 1(a), where the layer consists of a Se-Sn-Se slab. The distance between the adjacent layers is about 6.13 Å, which is greater than the Sn-Se bonding within the layer. For comparison, XRD was carried out in intercalated crystals. Figures 1(c) and 1(d) present the x-ray diffraction patterns for intercalated and as-grown crystals in the flat plane, respectively. Note that, in both cases, all peaks can be indexed with (0 0 l) (l is an integer), indicating the high quality of single crystals. To identify any difference before and after the intercalation, we zoom in on the (0 0 4) peaks as shown in Figs. 1(e) and 1(f) for intercalated and as-grown crystals, respectively. Due to high resolution, both $K\alpha_1$ and $K\alpha_2$ rays result in a (0 0 4) doublet. Compared to the as-grown crystal [Fig. 1(f)], the peak doublet for the intercalated crystal shifts to the left. Further calculations indicate that $c \sim 6.129 \pm 0.001$ Å for the as-grown $SnSe_2$ and ~6.134 ± 0.001 Å for Li_xSnSe_2. Increasing the solution concentration, duration, and current does not increase the c value. As discussed later, such small difference in the c parameter implies that (1) the Li concentration is low and (2) Li is located more interstitially than between layers as illustrated in Fig. 1(b). Due to the strong electronegativity of Se, it is energetically favorable for Li to occupy the interlayer space, surrounded by Se. The subtle lattice parameter change is extremely surprising as intercalation of other ions can double [43] or even triple [24] the interlayer spacing.

With negligible structure change, one would wonder if there was any impact in physical properties after intercalation. Figure 2(a) shows the temperature dependence of the in-plane resistivity (ρ_{ab}) of $SnSe_2$. From room temperature down to about 110 K, the resistivity decreases from ρ_{ab}(300 K) ~ 0.98 Ω cm to ρ_{ab}(110 K) ~ 0.57 Ω cm, which can be described by the Bloch-Grüneisen (BG) formula $\rho_{ab}(T) = \rho_{ab}(0) + B_{e-\mathrm{ph}}(\frac{T}{\Theta_D})\int_0^{\Theta_D/T}\frac{x^5}{(e^x-1)(1-e^{-x})}dx$. From the fit, we obtain the electron-phonon scattering strength $B_{e-\mathrm{ph}} \sim 2.2\Omega$ cm, the Debye temperature $\Theta_D \sim 180$ K, and $\rho_{ab}(0) \sim 0.072\,\Omega$ cm. Below ~110 K, the system changes into a nonmetallic state marked by an increase in the resistivity with decreasing temperature. By plotting the low-temperature data as $\ln(\rho_{ab})$ versus $1/T$ as shown in the inset, the linear behavior is revealed, which allows one to estimate the activation energy E_0 via $\rho_{ab}(T) = Ae^{E_0/2k_BT}$, where A is a constant and k_B is the Boltzmann constant. The fit of data between 20 and 45 K gives $E_0 \sim 23.8$ meV, which is much smaller than the theoretical value [43,44]. On the other hand, the c-axis resistivity (ρ_c) increases with decreasing temperature in the entire temperature range measured. Nevertheless, the resistivities, ρ_{ab} and ρ_c, obtained from intercalated crystals, as shown in Fig. 2(b), exhibit very different behavior. (1) ρ_{ab} of Li_xSnSe_2 decreases with decreasing temperature down to 20 mK, indicating metallic behavior in the entire measured temperature range. (2) The resistivity at room temperature is three orders smaller than that for an as-grown sample with ρ_{ab}(300 K) ~ 622 μΩ cm. (3) The resistivity drops quickly down to zero below 6 K. (4) ρ_c changes not only in magnitude but also in temperature dependence, revealing a peak around 35 K. These differences indicate that the intercalated crystals are different from that of as-grown samples, even though the interlayer spacing shows little change.

Quantitatively, ρ_{ab} of Li_xSnSe_2 can be well fitted by the BG formula between 300 and 32 K with $B_{e-\mathrm{ph}} \sim 525\mu\Omega$ cm and $\Theta_D \sim 105$ K. These values are much smaller than that

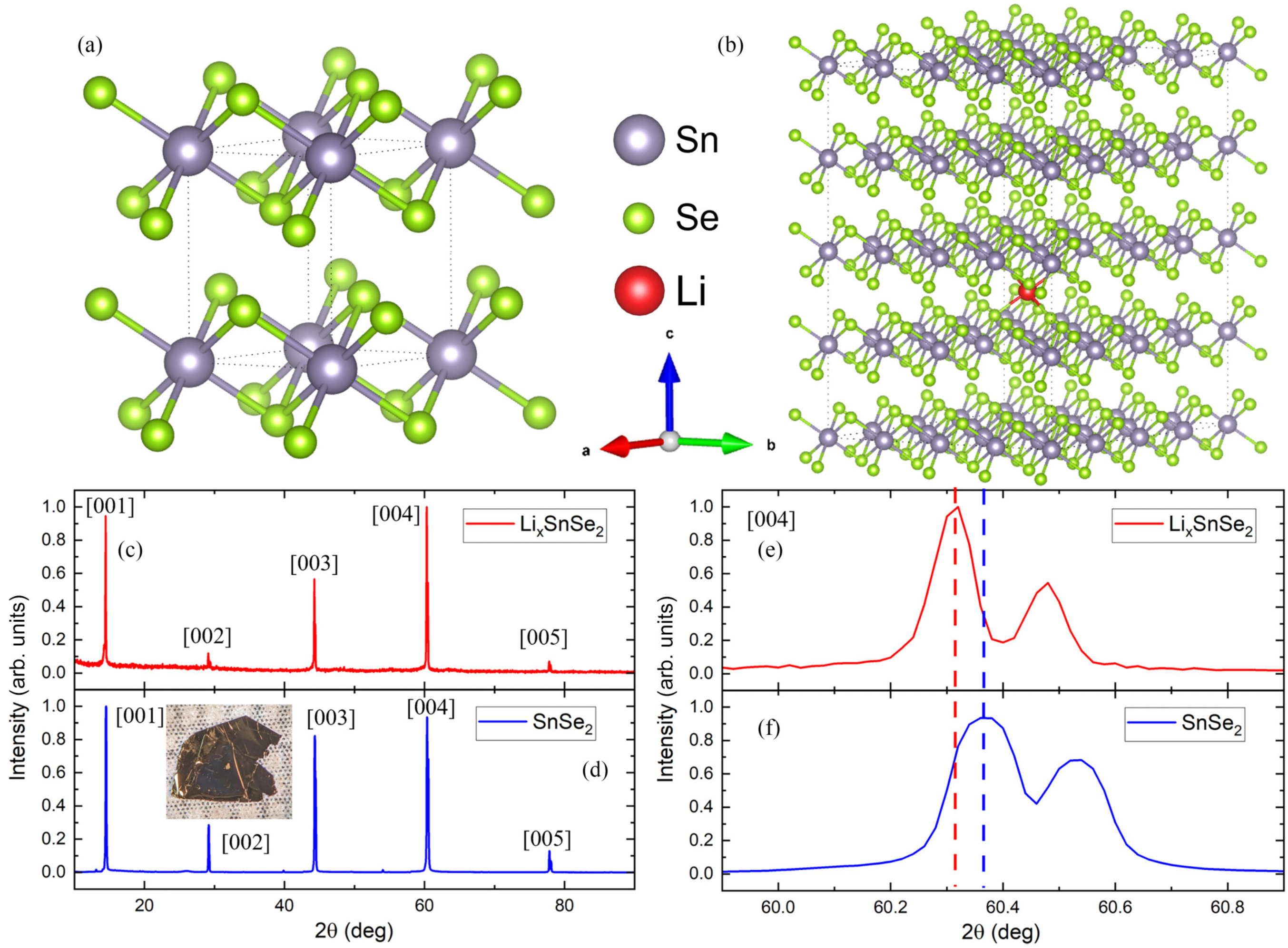

FIG. 1. (a), (b) Crystal structure of $SnSe_2$ and Li_xSnSe_2 (a $5 \times 5 \times 5$ supercell). (c), (d) Single-crystal diffraction patterns of $SnSe_2$, (d) Li_xSnSe_2 (c). (e), (f) Zoomed-in (004) peak for the intercalated (e) and unintercalated (f) cases.

obtained for $SnSe_2$, implying the change of electronic and phonon structures. The smaller Debye temperature reflects phonon softening in the intercalated crystals. On the other hand, since the fit of ρ_{ab} for $SnSe_2$ and Li_xSnSe_2 is in a different temperature range, there may be large uncertainties in fitting parameters. As shown below, the Debye temperature of Li_xSnSe_2 obtained from the specific heat is much higher than 105 K. Nevertheless, in Fig. 2(c), we plot the low-temperature resistivity data as ρ_{ab} versus T^2, revealing linear behavior between 7 and 30 K. It can thus be fitted using $\rho_{ab}(T) = \rho_{ab,0} + A'T^2$ with $\rho_{ab,0} = 76.7\mu\Omega\,\text{cm}$ and $A' = 0.03\mu\Omega\,\text{cm/K}^2$. The T^2 dependence of the resistivity in a nonmagnetic system indicates the Fermi liquid behavior with dominant electron-electron scattering at low temperatures. This is in sharp contrast with that seen in $SnSe_2$ with the nonmetallic ground state. Furthermore, ρ_{ab} of Li_xSnSe_2 drops to zero starting at $T_c^{\text{onset}} = 6.0$ K and ρ_c shows slightly lower T_c, as shown in Fig. 2(d). Such feature suggests the c-axis resistivity starts to drop when sufficient Cooper pairs are formed, at which the in-plane resistivity already reaches zero. The observation of the zero-resistivity state in ρ_c indicates that Li intercalation penetrates to the bulk single crystals, leading to 3D superconductivity.

To confirm the superconducting transition, the magnetic properties need to be investigated. Figure 2(e) presents the temperature dependence of the magnetic susceptibility measured by applying the magnetic field $H//c$ with $H = 1$ T for both as-grown $SnSe_2$ and intercalated Li_xSnSe_2. In both cases, the c-axis susceptibility χ_c is negative in the entire measured temperature range. This suggests the dominant core contribution, which is diamagnetic. Compared to that for the as-grown crystals, χ_c for Li_xSnSe_2 is less negative, because of positive contribution from free electrons. To understand the zero-resistivity state shown in Fig. 2(d), we measure the temperature dependence of the magnetic susceptibility of Li_xSnSe_2 under 10 Oe between 1.8 and 10 K. As shown in Fig. 2(f), a strong diamagnetic signal develops below $T_c^{\text{onset}} = 6.0$ K for both the zero field cooling (ZFC) and field cooling (FC) conditions. With decreasing temperature, both χ_{ZFC} and χ_{FC} continuously decrease with $4\pi\chi_{\text{FC}} \sim -0.07$ and $4\pi\chi_{\text{ZFC}} \sim -0.65$ at $T = 2$ K. Both the zero resistivity and diamagnetism below T_c^{onset} indicate the entrance to the superconducting state. At 2 K, the superconducting volume is ∼7% based on $4\pi\chi_{\text{FC}}$, while $4\pi\chi_{\text{ZFC}}$ reaches ∼65% [45]. The ratio $\chi_{\text{FC}}/\chi_{\text{ZFC}}$ is much larger than that for the molecularly intercalated case which is ∼0.06

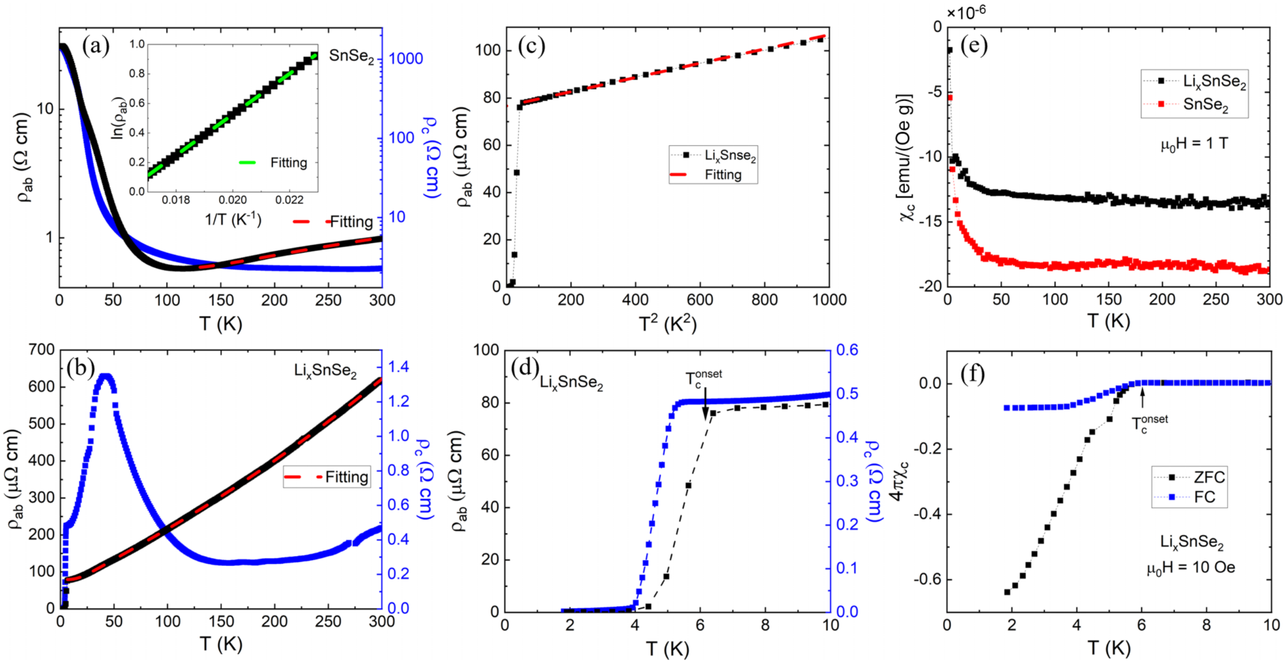

FIG. 2. (a) Temperature dependence of the in-plane (ρ_{ab}) and out-of-plane (ρ_c) electrical resistivity of $SnSe_2$. The red dashed line is the fit of metallic ρ_{ab} to the Bloch-Grüneisen formula. Inset: $\rho_{ab}(T)$ plotted as $\ln(\rho_{ab})$ versus $1/T$, showing the linear relationship. (b) Temperature dependence of the in-plane (ρ_{ab}) and out of plane (ρ_c) electrical resistivity of Li_xSnSe_2. (c) Temperature dependence of the normal-state ρ_{ab} for Li_xSnSe_2 plotted as ρ_{ab} versus T^2 below 33 K. (d) Temperature dependence of ρ_{ab} and ρ_c of Li_xSnSe_2 between 1.8 and 10 K. (e) Temperature dependence of the magnetic susceptibility for Li_xSnSe_2 (black squares) and $SnSe_2$ (red squares) taken by applying $H = 1$ T along the c direction. (f) Temperature dependence of the magnetic susceptibility for Li_xSnSe_2 between 1.8 and 10 K at $H = 10$ Oe under both zero field cooling (ZFC) and field cooling (FC) modes.

[24]. The latter was considered as two-dimensional (2D) superconductivity [24].

Figure 3(a) presents the temperature dependence of $\rho_{ab}(T)$ between 20 mK and 10 K measured at various fields for Li_xSnSe_2. With increasing H, the superconducting transition is pushed to lower temperatures. At 1 T, $\rho_{ab}(T)$ becomes completely flat down to 20 mK. We determine the transition temperature at each field $T_c(H)$ based on the 10%, 50%, and 90% resistivity drop with respect to the normal-state resistivity ($\rho_{ab}^{\rm norm}$). Figure 3(b) shows the $T_c(H)$ values plotted as the temperature dependence of the upper critical field (H_{c2}^c). For H_{c2}^c obtained from either 90% $\rho_{ab}^{\rm norm}$ or 50% $\rho_{ab}^{\rm norm}$, its temperature dependence is nearly linear in the entire phase diagram, consistent with that seen close to T_{c0} [22–24]. Interestingly, $H_{c2}^c(T)$ obtained from 10% $\rho_{ab}^{\rm norm}$ can be well fitted by the empirical formula, $H_{c2}(T) = H_{c2}(0)[1 - (\frac{T}{T_{c0}})^2]$, as demonstrated by the red dashed line in Fig. 3(b). The fit gives $H_{c2}^c(0) = 754$ Oe. Using the Ginzburg-Landau formula, we can further estimate the in-plane coherence length $\xi_{\rm GL}^{ab} = \sqrt{\frac{\varphi_0}{2\pi H_{c2}^c(0)}} \sim 66.1$ nm ($\varphi_0 = h/2e$).

The linear temperature dependence of the upper critical field applied normal to the superconducting plane is the signature of 2D superconductivity [22,24,46]. The fact that $H_{c2}^c(T)$ obtained from 10% $\rho_{ab}^{\rm norm}$ follows the quadratic temperature dependence suggests that the occurrence of linear H_{c2}^c (90% $\rho_{ab}^{\rm norm}$) and H_{c2}^c (50% $\rho_{ab}^{\rm norm}$) in our system has the same origin, i.e., with the initial in-plane superconductivity only, which is also reflected in slightly lower T_c determined from the c-axis resistivity. To confirm, we estimate critical fields through the magnetization, which represents the bulk measurements. Figure 3(c) shows the field dependence of the magnetization at indicated temperatures, where H is applied along the ab plane. At each temperature, we define the in-plane upper critical field H_{c2}^{ab} when the magnetization departs from the high-temperature behavior [represented by a dashed line in Fig. 3(c)] and the in-plane lower critical field H_{c1}^{ab} when the magnetization deviates from the low-field linearity. The temperature dependence of H_{c1}^{ab} (green) and H_{c2}^{ab} (red) is plotted in Fig. 3(d) as a function of T/T_{c0}. Interestingly, both $H_{c1}^{ab}(T)$ and $H_{c2}^{ab}(T)$ can be described by the aforementioned empirical formulas as illustrated by dashed curves in Fig. 3(d). The fitting gives $H_{c1}^{ab}(0) \sim 27$ Oe and $H_{c2}^{ab}(0) \sim 1652$ Oe. Using the GL formula $H_{c2}^{ab} = \frac{\varphi_0}{2\pi \xi_{\rm GL}^{ab} \xi_{\rm GL}^c}$, we can estimate the c-axis coherence length $\xi_{\rm GL}^c \sim 30.3$ nm. Furthermore, from the relationship $H_{c1}^{ab} = \frac{\varphi_0}{4\pi \lambda_c^2} \ln(\frac{\lambda_c}{\xi_{\rm GL}^c})$, we can estimate the c-axis penetration depth $\lambda_c \sim 396$ nm, which is much larger than $\xi_{\rm GL}^c$.

From the above superconducting parameters, it is clear that Li_xSnSe_2 is a type-II superconductor with the Ginzburg-Landau parameter $\lambda_c/\xi_{\rm GL}^c \sim 13$. The superconducting anisotropy can be estimated via $\xi_{\rm GL}^{ab}/\xi_{\rm GL}^c \sim 2.2$. This is much smaller than the anisotropy in $[DEMB]^+$ intercalated $SnSe_2$ (∼8.8) [23] and Li intercalated $SnSe_2$ flakes (∼11) [22]. While a small superconducting anisotropy was also reported in $[Co(Cp)_2]$ intercalated $SnSe_2$ [47], it is not clear how this is possible as the insertion of $[Co(Cp)_2]$ nearly doubles the interlayer distance [13]. Nevertheless, from what is shown in Fig. 3, the superconducting state is well established in our Li_xSnSe_2 with 3D characteristics.

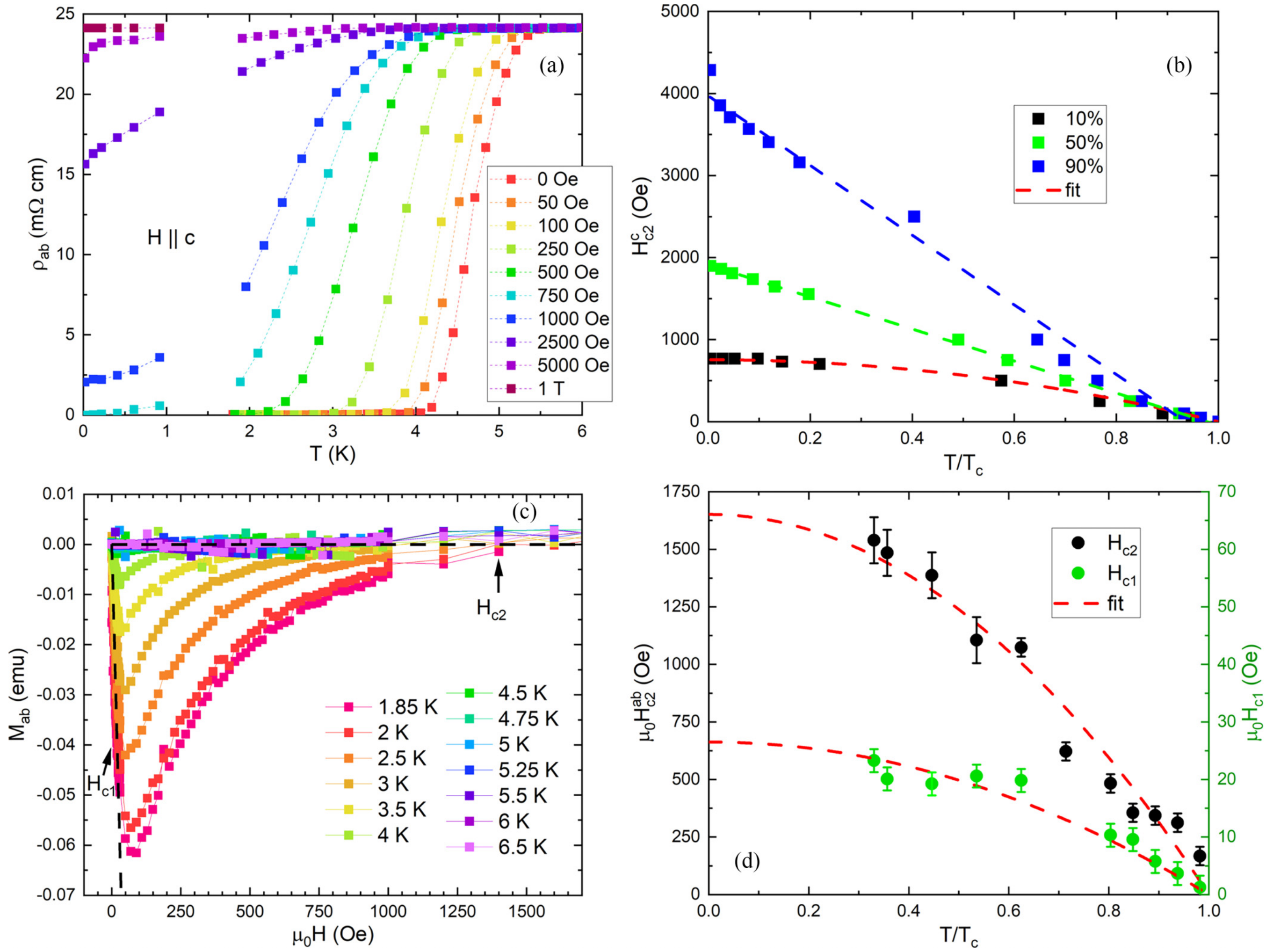

FIG. 3. (a) Temperature dependence of the in-plane electrical resistivity measured under indicated applied magnetic fields ($H||c$) for Li_xSnSe_2. (b) Temperature dependence of the upper critical field ($\mu_0 H_{c2}^c$) corresponding to 90% ρ_{ab} (blue squares), 50% ρ_{ab} (green squares), and 10% ρ_{ab} (black squares) for Li_xSnSe_2. The dashed red line is the fit of data to the empirical formula (see text); dashed green and blue lines are guide to eyes. (c) Field dependence of the in-plane magnetization at indicated temperatures for Li_xSnSe_2. (d) Upper critical field ($\mu_0 H_{c2}^{ab}$) and lower critical field ($\mu_0 H_{c1}^{ab}$) versus temperature for Li_xSnSe_2. The dashed red lines are the fit of data to the empirical formula (see text).

Given that there is very little change in the crystal structure [see Fig. 1(e)], one may wonder how the ground state is changed from the nonmetallic ground state in the as-grown system to the superconducting state in the intercalated system. To answer the question, we measure the Hall resistivity (ρ_{xy}) for $SnSe_2$ and Li_xSnSe_2. Figures 4(a) and 4(b) show the field dependence of ρ_{xy} for as-grown $SnSe_2$ and intercalated Li_xSnSe_2 in the indicated temperatures. For as-grown $SnSe_2$, $\rho_{xy}(H)$ exhibits linear behavior between 0 and 14 T. The exception is $\rho_{xy}(H)$ at 50 K, which deviates from linearity above $H > 6$ T. We fit data using $\rho_{xy}(H) = R_H \mu_0 H$ in the linear regime ($H < 6$ T), with the Hall coefficient R_H shown in Fig. 4(c). Between 1.8 and 300 K, R_H is negative with its amplitude initially increasing with decreasing temperature. It decreases again after reaching the maximum at 50 K. For Li_xSnSe_2, $\rho_{xy}(H)$ exhibits linear behavior between 0 and 14 T at all temperatures measured. R_H can then be easily extracted, which is also negative between 1.8 and 300 K as shown in Fig. 4(d). Note that the amplitude of R_H for Li_xSnSe_2 decreases with decreasing temperature with slight increase below ∼30 K.

The negative R_H implies dominant electron carriers in both as-grown $SnSe_2$ and intercalated Li_xSnSe_2. To estimate the carrier concentration n, we use $R_H = -\frac{1}{ne}$, which is for the single-band systems (where e is electron charge). The temperature dependence of the carrier concentration n is shown in Figs. 4(c) and 4(d) for $SnSe_2$ and Li_xSnSe_2, respectively. It is worth noting that the carrier concentration has increased by two orders of magnitude after the intercalation. This clearly demonstrates the existence of Li^+ in the intercalated crystals. Based on the carrier concentration at 300 K, we estimate that the Li concentration $x < 0.02\%$.

Difference between the as-grown and intercalated systems can also be seen in the specific heat. Figure 5(a) shows the low-temperature specific heat (C) plotted as C/T versus T^2 for both as-grown $SnSe_2$ and intercalated Li_xSnSe_2, respectively. For $SnSe_2$, $C/T(T^2)$ exhibits linear behavior below ∼7 K. We fit data using $C/T = \gamma + \beta T^2$, where γ is the

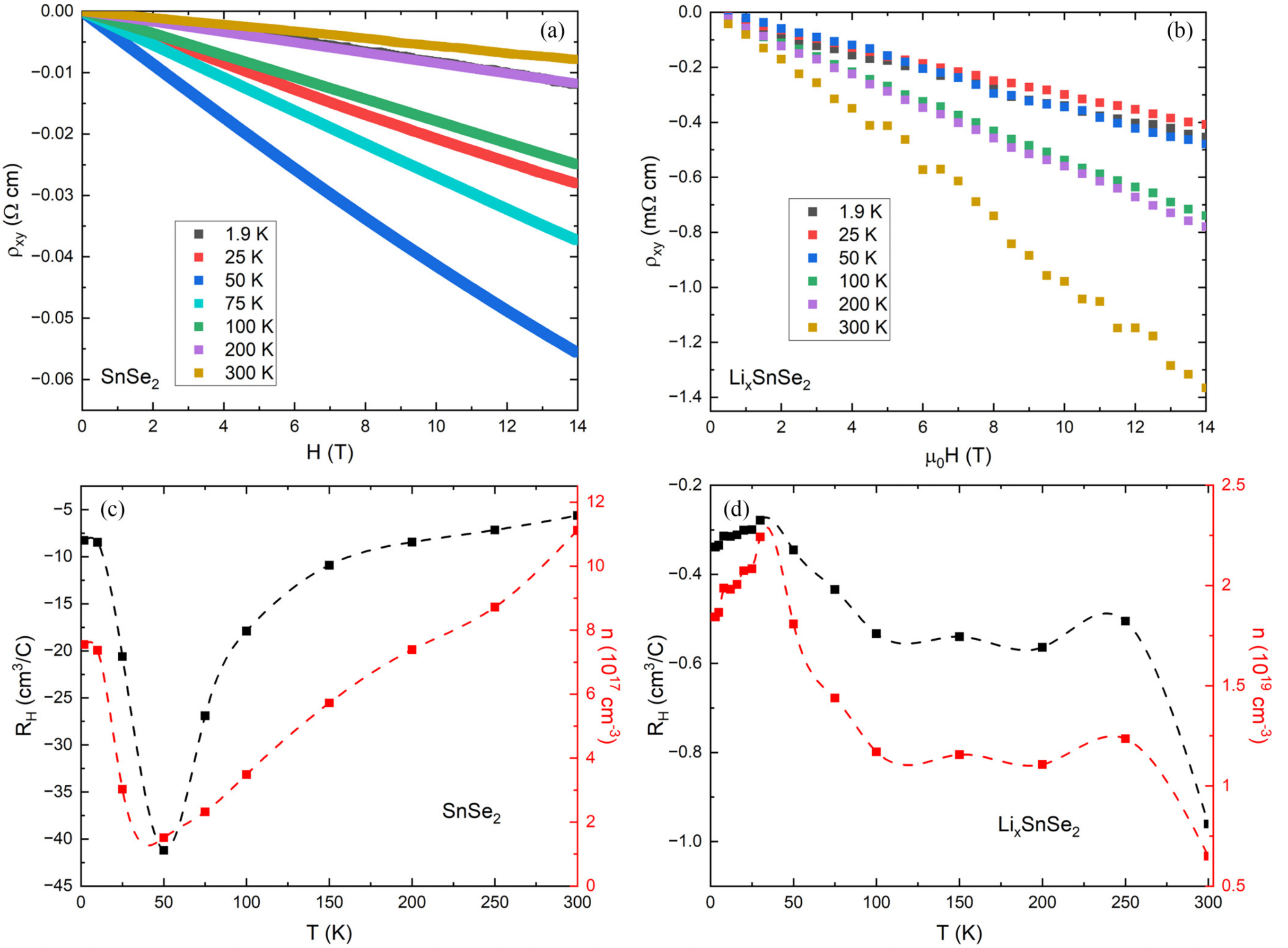

FIG. 4. (a), (b) Magnetic field dependence of the Hall resistivity (ρ_{xy}) measured between 1.8 and 300 K for $SnSe_2$ (a) and Li_xSnSe_2 (b). (c) Temperature dependence of the Hall coefficient (R_H) for $SnSe_2$ (black squares) and Li_xSnSe_2 (red squares). (d) Temperature dependence of the carrier concentration for $SnSe_2$ (black squares) and Li_xSnSe_2 (red squares).

electronic specific heat coefficient and $\beta = \frac{12\pi^4 N k_B}{5\theta_D^3}$ with k_B the Boltzmann constant, and N the atomic number of the unit cell. The fit results in $\gamma(SnSe_2) = 0$ and $\theta_D(SnSe_2) = 190$ K. The zero $\gamma(SnSe_2)$ is consistent with the semiconducting ground state of $SnSe_2$. The Debye temperature is close to that obtained from fitting the metallic ρ_{ab}. For the intercalated system, C/T is enhanced, resulting in a larger slope above and below T_c. The corresponding $\theta_D(Li_xSnSe_2) = 175$ K, softer than that of $SnSe_2$. This again indicates the effect of Li on the crystal structure. Note that the intercept $\gamma_N(Li_xSnSe_2) \sim 3.4$ mJ/mol K^2 at $T > T_c$, but $\gamma_{residual}(Li_xSnSe_2) \sim 0$ at $T < T_c$. The difference that should be attributed to the superconducting transition. Due to small superconducting volume, the specific heat peak is absent. We emphasize that the absence of the specific heat peak is not in contradiction with 3D superconductivity discussed above. As described in Ref. [47], organometallic intercalate $SnSe_2[Co(ETA - C_5H_5)_2]_{0.3}$ results in more 3D and less anisotropic superconductivity as well. Our data for superconducting Li_xSnSe_2 support such claim.

Based on the above comparative study, it is obvious that Li intercalation results in drastic physical properties changes both in plane and out of plane. Figure 5(b) shows the magnetic field dependence of ρ_{ab} at $T = 20$ mK with field direction rotating from 0° ($H//c$) to 90° ($H//ab$). At all measured angles, after the initial rise due to the suppression of superconductivity, $\rho_{ab}(H)$ increases more or less linearly without any sign of saturation up to 18 T. According to Abrikosov theory [48], the linear field dependence of the resistivity occurs in the quantum limit due to the linear energy-momentum dispersion relationship. Unfortunately, the absence of quantum oscillations prevents the assessment of the quantum limit experimentally.

According to the recent systematic study, there is a simple relationship between the intercalated single-element concentration x and T_c [49]. For Li_xSnSe_2 with $T_c = 6.0$ K, the x value is expected to be of the order of $\sim$0.1 [48]. However, our Hall effect data give a three orders of magnitude lower x. To figure out how an extremely small amount of Li intercalation makes a drastic property change, we perform relativistic band structure calculations by placing one Li atom in $2 \times 2 \times 2$ (222), $3 \times 3 \times 3$ (333), $4 \times 4 \times 4$ (444), and $5 \times 5 \times 5$ [555; see Fig. 1(b)] supercells. Figure 5(c) shows the band structure of the 333 supercell with $\sim$1.2% Li

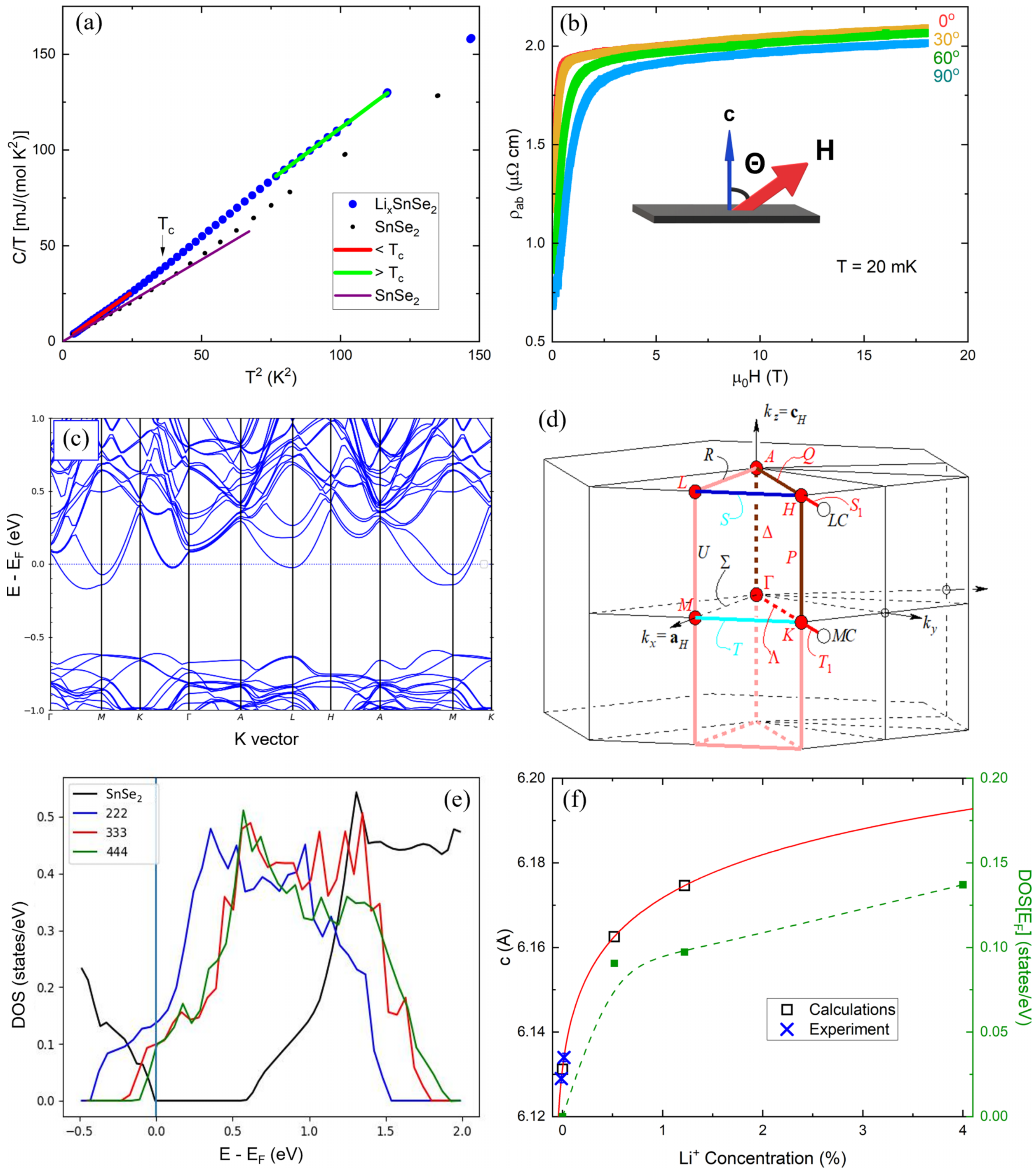

FIG. 5. (a) Low-temperature specific heat (C) plotted as C/T versus T^2 for as-grown $SnSe_2$ (black filled circles) and intercalated Li_xSnSe_2 (blue circles). The brown solid line is the linear fit of $C/T(T^2)$ for $SnSe_2$ below 6 K. The red and green lines represent linear fit of $C/T(T^2)$ for Li_xSnSe_2 below and above T_c, respectively. (b) Field dependence of ρ_{ab} under different field directions ($\theta = 0°$, 30°, 60°, and 90°) at $T = 20$ mK. (c) Electronic structure of the $3 \times 3 \times 3$ supercell (1.2% Li concentration). (d) Brillouin zone. (e) Calculated density of states (DOS) versus energy for different Li concentrations, i.e., one Li atom in $2 \times 2 \times 2$ (222), $3 \times 3 \times 3$ (333), and $4 \times 4 \times 4$ (444) supercells, respectively. (f) Calculated c-axis lattice parameter and DOS(E_F) versus Li concentration. Crosses represent data from experiment.

concentration. Both Sn and Se bands cross the Fermi level (E_F) centered at M and L and between K and Γ [see the Brillouin zone presented in Fig. 5(d)]. This implies the metallicity in the 1.2% Li doped system. Figure 5(e) shows the Li concentration dependence of the density of states [DOS(E)] for the undoped (marked as 111), 222, 333, and 444 supercells. As soon as Li is introduced, the DOS at E_F becomes finite, implying that the system becomes metallic [see Fig. 5(f)]. The finite DOS ($E - E_F = 0$) results mostly from Sn, consistent with previous calculations [21]. This is different from the pressure effect. According to Ref. [25], pressure-induced superconductivity in $SnSe_2$ is due to strong Se-Se bonding, providing finite DOS at the Fermi level. This implies that $SnSe_2$ is an extremely sensitive system, susceptible to any perturbation. Figure 5(f) displays the calculated c lattice parameter at various Li concentration (squares). Based on our experimentally obtained c value, we estimate $x \sim 0.017\%$, consistent with our estimate from the Hall effect. At this doping level, DOS is barely nonzero.

Through the combined experimental and computational investigation, it becomes clear that superconductivity can be induced in $SnSe_2$ through multiple approaches by (1) intercalation with noticeable interlayer expansion, (2) compression with enhanced Se-Se bonding, and (3) an extremely small amount of doping with negligible structure change which is from this work. The enhanced interlayer separation is considered to soften phonons to enhance the electron-phonon coupling [21]. In our case, there is a slight decrease of the Debye temperature from 190 K for $SnSe_2$ to 175 K for Li_xSnSe_2, which is difficult to count for the enhanced electron-phonon coupling. In fact, the in-plane resistivity of Li_xSnSe_2 can be perfectly fitted by the T^2 dependence between T_c and ∼30 K implying predominantly electron-electron interaction at low temperatures. This points to the scenario proposed in Ref. [44] that charge fluctuation may be responsible for Cooper pairing in Li_xSnSe_2. The observation of superconductivity along both the in-plane and c direction could be the consequence of charge fluctuation.

IV. CONCLUSION

Superconducting Li_xSnSe_2 single crystals were prepared through electrochemical intercalation. Both the electrical resistivity and magnetic susceptibility indicate the superconducting transition temperature $T_c \sim 6.0$ K. Through in-plane resistivity measurements down to 20 mK and magnetic susceptibility measurements down to 1.8 K, we construct the lower critical field (H_{c1}^{ab}) and upper critical field (H_{c2}^{ab} and H_{c2}^{c}) diagrams. While H_{c2}^{c} obtained from 90% ρ_{ab}^{norm} and 50% ρ_{ab}^{norm} exhibits linear temperature dependence, H_{c2}^{c} (90% ρ_{ab}^{norm}), and $H_{c1}^{ab}(M)$ and H_{c2}^{ab} (M) can be described by the empirical formula $H_{ci}(T) = H_{ci}(0)[1 - (T/T_{c0})^2 (i = 1, 2)$, giving $H_{c2}^{c}(0) = 754$ Oe, $H_{c1}^{ab}(0) = 27$ Oe, and $H_{c2}^{ab}(0) = 1652$ Oe. Using the Ginzburg-Landau formula, we further estimate that the c-axis penetration depth $\lambda_c(0) = 396$ nm and the coherence length anisotropy $\xi_{ab}(0) = 66.1$ nm and $\xi_c(0) = 30.3$ nm. The fact that $\xi_c(0)$ is much longer than the interlayer separation implies 3D superconductivity, consistent with the observation of the zero-resistivity state of ρ_c, the electronic specific heat change at T_c, and small superconducting anisotropy.

What is most remarkable is the extremely small amount of Li concentration in superconducting Li_xSnSe_2 with $x \sim 1.7\times10^{-4}$, based on the estimate from the c-axis lattice parameter, carrier concentration, and first-principles calculations. This is three orders of magnitude lower than the required superconductivity onset condition [47]. Such low-doping-induced superconductivity could serve as a model system for studying unconventional superconducting mechanisms such as charge fluctuation mediated Cooper pairing [14], as there is the minimum change of the crystal structure. The perfect T^2 dependence of the in-plane resistivity down to T_c suggests the importance of electron-electron interaction.

ACKNOWLEDGMENT

This work was partially (D.D., E.T., W.A.S., R.J.) supported by the Department of Energy through Grant No. DE-SC0024501.

[1] C. C. Tsuei and J. R. Kirtley, Pairing symmetry in cuprate superconductors, Rev. Mod. Phys. **72**, 969 (2000).

[2] D. Li, K. Lee, B. Y. Wang, M. Osada, S. Crossley, H. R. Lee, Y. Cui, Y. Hikita, and H. Y. Hwang, Superconductivity in an infinite-layer nickelate, Nature (London) **572**, 624 (2019).

[3] P. J. Hirschfeld, M. M. Korshunov, and I. I. Mazin, Gap symmetry and structure of Fe-based superconductors, Rep. Prog. Phys. **74**, 124508 (2011).

[4] M. Yankowitz, S. Chen, H. Polshyn, Y. Zhang, K. Watanabe, T. Taniguchi, D. Graf, A. F. Young, and C. R. Dean, Tuning superconductivity in twisted bilayer graphene, Science **363**, 1059 (2019).

[5] H. Sun, M. Huo, X. Hu, J. Li, Z. Liu, Y. Han, L. Tank, Z. Mao, P. Yang, B. Wang, J. Cheng, D.-Y. Yao, G.-M. Zhang, and M. Wang, Signatures of superconductivity near 80 K in a nickelate under high pressure, Nature (London) **621**, 493 (2023).

[6] M. Zhang, C. Pei, X. Du, Y. Cao, Q. Wang, J. Wu, Y. Li, Y. Zhao, C. Li, W. Cao, S. Zhu, Q. Zhang, N. Yu, P. Cheng, J. Zhao, Y. Chen, H. Guo, L. Yang, and Y. Qu, Superconductivity in trilayer nickelate $La_4Ni_3O_{10}$ under pressure, arXiv:2311.07423.

[7] K. Takada, H. Sakurai, E. Takayama-Muromachi, F. Izumi, R. A. Dilanian, and T. Sasaki, Superconductivity in two-dimensional CoO_2 layers, Nature (London) **422**, 53 (2003).

[8] R. Jin, B. C. Sales, P. Khalifah, and D. Mandrus, Observation of bulk superconductivity in $Na_xCoO_2 \cdot yH_2O$ and $Na_xCoO_2 \cdot yD_2O$ powder and single crystals, Phys. Rev. Lett. **91**, 217001 (2003).

[9] H. Ikeda, Y. Nisikawa, and K. Yamada, Possibility of f-wave spin-triplet superconductivity in the CoO_2 superconductor: A case study on a 2D triangular lattice in the repulsive Hubbard model, J. Phys. Soc. Jpn. **73**, 17 (2003).

[10] I. I. Mazin and M. D. Johannes, A critical assessment of the superconducting pairing symmetry in $Na_xCoO_2 \cdot yH_2O$, Nat. Phys. **1**, 91 (2005).

[11] Y. Yanase, M. Mochizuki, and M. Ogata, Multi-orbital analysis on the superconductivity in $Na_xCoO_2 \cdot yH_2O$, J. Phys. Soc. Jpn. **74**, 430 (2005).

[12] J. An, H. Q. Lin, and D. Gong, Coexistence of f-wave superconductivity, charge order, and spin antiferromagnetism around nonmagnetic impurities in $Na_{0.33}CoO_2 \cdot 1.3H_2O$, Phys. Rev. Lett. **96**, 227001 (2006).

[13] Z. Li, Y. Zhao, K. Mu, H. Shan, Y. Guo, J. Wu, Y. Su, Q. Wu, Z. Sun, A. Zhao, X. Cui, C. Wu, and Y. Xie, Molecule-confined engineering toward superconductivity and ferromagnetism in two-dimensional superlattice, J. Am. Chem. Soc. **139**, 16398 (2017).

[14] Y. X. Li, Z. J. Yao, S. L. Yu, and J. X. Li, Superconductivity and density-wave fluctuations in an extended triangular Hubbard model: An application to $SnSe_2$, J. Phys.: Condens. Matter **35**, 045602 (2023).

[15] E. Morosan, H. W. Zandbergen, B. S. Dennis, J. W. G. Bos, Y. Onose, T. Klimczuk, A. P. Ramirez, N. P. Ong, and R. J. Cava, Superconductivity in Cu_xTiSe_2, Nat. Phys. **2**, 544 (2006).

[16] J. F. Zhao, H. W. Ou, G. Wu, B. P. Xie, Y. Zhang, D. W. Shen, J. Wei, L. X. Yang, J. K. Dong, M. Arita, H. Namatame, M. Taniguchi, X. H. Chen, and D. L. Feng, Evolution of the electronic structure of $1T$-Cu_xTiSe_2, Phys. Rev. Lett. **99**, 146401 (2007).

[17] A. F. Kusmartseva, B. Sipos, H. Berger, L. Forró, and E. Tutiš, Pressure induced superconductivity in pristine $1T$-$TiSe_2$, Phys. Rev. Lett. **103**, 236401 (2009).

[18] E. Morosan, K. E. Wagner, L. L. Zhao, Y. Hor, A. J. Williams, J. Tao, Y. Zhu, and R. J. Cava, Multiple electronic transitions and superconductivity in Pd_xTiSe_2, Phys. Rev. B **81**, 094524 (2010).

[19] K. Sato, T. Noji, T. Hatakeda, T. Kawamata, M. Kato, and Y. Koike, New lithium- and diamines-intercalated superconductors $Li_x(C_2H_8N_2)_yTiSe_2$ and $Li_x(C_6H_{16}N_2)_yTiSe_2$, J. Phys. Soc. Jpn. **86**, 104701 (2017).

[20] M. Liao, H. Wang, Y. Zhu, R. Shang, M. Rafique, L. Yang, H. Zhang, D. Zhang, and Q.-K. Xue, Coexistence of resistance oscillations and the anomalous metal phase in a lithium intercalated $TiSe_2$ superconductor, Nat. Commun. **12**, 5342 (2021).

[21] Y. Song, X. Liang, J. Guo, J. Deng, G. Gao, and X. Chen, Superconductivity in Li-intercalated $1T$-$SnSe_2$ driven by electric field gating, Phys. Rev. Mater. **3**, 054804 (2019).

[22] J. Zeng, E. Liu, Y. Fu, Z. Chen, C. Pan, C. Wang, M. Wang, Y. Wang, K. Xu, S. Cai, X. Yan, Y. Wang, X. Liu, P. Wang, S. J. Liang, Y. Cui, H. Y. Hwang, H. Yuan, and F. Miao, Gate-induced interfacial superconductivity in $1T$-$SnSe_2$, Nano Lett. **18**, 1410 (2018).

[23] A. Rousuli, H. Zhang, K. Zhang, H. Zhong, R. Feng, Y. Wu, P. Yu, and S. Zhou, Induced anisotropic superconductivity in ionic liquid cation intercalated $1T$-$SnSe_2$, 2D Mater. **8**, 015024 (2021).

[24] L. K. Ma, M. Z. Shi, B. L. Kang, K. L. Peng, F. B. Meng, C. S. Zhu, J. H. Cui, Z. L. Sun, D. H. Ma, H. H. Wang, B. Lei, T. Wu, and X. H. Chen, Quasi-two-dimensional superconductivity in $SnSe_2$ via organic ion intercalation, Phys. Rev. Mater. **4**, 124803 (2020).

[25] S. Zhang, R. A. Susilo, S. Wan, W. Deng, B. Chen, and C. Gao, Origin of the decompression driven superconductivity enhancement in $SnSe_2$, J. Mater. Chem. C **11**, 12254 (2023).

[26] G. Kresse and J. Hafner, *Ab initio* molecular dynamics for liquid metals, Phys. Rev. B **47**, 558 (1993).

[27] G. Kresse and J. Hafner, *Ab initio* molecular-dynamics simulation of the liquid-metal-amorphous-semiconductor transition in germanium, Phys. Rev. B **49**, 14251 (1994).

[28] G. Kresse and J. Furthmüller, Efficient iterative schemes for *ab initio* total-energy calculations using a plane-wave basis set, Phys. Rev. B **54**, 11169 (1996).

[29] G. Kresse and D. Joubert, From ultrasoft pseudopotentials to the projector augmented-wave method, Phys. Rev. B **59**, 1758 (1999).

[30] P. E. Blöchl, Projector augmented-wave method, Phys. Rev. B **50**, 17953 (1994).

[31] J. P. Perdew, K. Burke, and M. Ernzerhof, Generalized gradient approximation made simple, Phys. Rev. Lett. **77**, 3865 (1996).

[32] S. Grimme, Semiempirical GGA-type density functional constructed with a long-range dispersion correction, J. Comput. Chem. **27**, 1787 (2006).

[33] S. Grimme, J. Antony, S. Ehrlich, and H. Krieg, A consistent and accurate *ab initio* parametrization of density functional dispersion correction (DFT-D) for the 94 elements H–Pu, J. Chem. Phys. **132**, 154104 (2010).

[34] S. Grimme, S. Ehrlich, and L. Goerigk, Effect of the damping function in dispersion corrected density functional theory, J. Comput. Chem. **32**, 1456 (2011).

[35] A. Tkatchenko and M. Scheffler, Accurate molecular van der Waals interactions from ground-state electron density and free-atom reference data, Phys. Rev. Lett. **102**, 073005 (2009).

[36] V. G. Ruiz, W. Liu, and A. Tkatchenko, Density-functional theory with screened van der Waals interactions applied to atomic and molecular adsorbates on close-packed and non-close-packed surfaces, Phys. Rev. B **93**, 035118 (2016).

[37] J. Klimeš, D. R. Bowler, and A. Michaelides, Chemical accuracy for the van der Waals density functional, J. Phys.: Condens. Matter **22**, 022201 (2010).

[38] J. Klimeš, D. R. Bowler, and A. Michaelides, Van der Waals density functionals applied to solids, Phys. Rev. B **83**, 195131 (2011).

[39] H. Peng, Z.-H. Yang, J. P. Perdew, and J. Sun, Versatile van der Waals density functional based on a meta-generalized gradient approximation, Phys. Rev. X **6**, 041005 (2016).

[40] J. Ning, M. Kothakonda, J. W. Furness, A. D. Kaplan, S. Ehlert, J. G. Brandenburg, J. P. Perdew, and J. Sun, Workhorse minimally empirical dispersion-corrected density functional with tests for weakly bound systems: $r^2SCAN + rVV10$, Phys. Rev. B **106**, 075422 (2022).

[41] C. Y. Fong and M. L. Cohen, Electronic energy-band structure of SnS_2 and $SnSe_2$, Phys. Rev. B **5**, 3095 (1972).

[42] A.-T. Pham, T. H. Vu, C. Cheng, T. L. Trinh, J.-E. Lee, H. Ryu, C. Hwang, S.-K. Mo, J. Kim, L-D. Zhao, A.-T. Duong, and S. Cho, High-quality $SnSe_2$ single crystals: Electronic and thermoelectric properties, Appl. Energy Mater. **3**, 10787 (2020).

[43] H. Wu, S. Li, M. Susner, S. Kwon, M. Kim, T. Haugan, and B. Lv, Spacing dependent and cation doping independent superconductivity in intercalated $1T$ 2D $SnSe_2$, 2D Mater. **6**, 045048 (2019).

[44] A. Rajbanshi, D. Duong, E. Thareja, B. A. Shelton, and R. Jin, Thermoelectric properties of SnSe and $SnSe_2$ single crystals, Phys. Rev. Mater. **8**, 023601 (2024).

[45] M. Thinkim, *Introduction to Superconductivity*, 2nd ed. (Dover Publications, Mineola, NY, 2004).
[46] V. L. Ginzburg and L. D. Landau, On the theory of superconductivity, in *On Superconductivity and Superfluidity* (Springer, Berlin, 2009).
[47] D. O'Hare, H. Wong, S. Hazell, and W. J. Hodby, Relatively isotropic superconductivity at 8.3-K in the Lamellar organometallic intercalate $SnSe_2(Co(\eta\text{-}C_5H_5)_2)_{0.3}$, Adv. Mater. **4**, 658 (1992).
[48] A. A. Abrikosov, Quantum magnetoresistance, Phys. Rev. B **58**, 2788 (1998).
[49] S. M. Benjamin, Estimating the single-element concentration of intercalated insulators for the emergence of superconductivity, ACS Phys. Chem. Au **2**, 108 (2022).